The Lamb shift in muonic hydrogen[1]

Randolf Pohl, Aldo Antognini, François Nez, Fernando D. Amaro, François Biraben, João M.R. Cardoso, Daniel S. Covita, Andreas Dax, Satish Dhawan, Luis M.P. Fernandes, Adolf Giesen, Thomas Graf, Theodor W. Hänsch, Paul Indelicato, Lucile Julien, Cheng-Yang Kao, Paul Knowles, Eric-Olivier Le Bigot, Yi-Wei Liu, José A.M. Lopes, Livia Ludhova, Cristina M.B. Monteiro, Françoise Mulhauser, Tobias Nebel, Paul Rabinowitz, Joaquim M.F. dos Santos, Lukas A. Schaller, Karsten Schuhmann, Catherine Schwob, David Taqqu, João F.C.A. Veloso, and Franz Kottmann

Abstract: The long quest for a measurement of the Lamb shift in muonic hydrogen is over. Last year we measured the energy splitting (Pohl et al., *Nature*, **466**, 213 (2010)) in μp with an experimental accuracy of 15 ppm, twice better than our proposed goal. Using current QED calculations of the fine, hyperfine, QED, and finite size contributions, we obtain a root-mean-square proton charge radius of $r_p = 0.841\,84\,(67)$ fm. This value is 10 times more precise, but 5 standard deviations smaller, than the 2006 CODATA value of r_p. The origin of this discrepancy is not known. Our measurement, together with precise measurements of the 1S–2S transition in regular hydrogen and deuterium, gives improved values of the Rydberg constant, $R_\infty = 10\,973\,731.568\,160\,(16)$ m^{-1} and the rms charge radius of the deuteron $r_d = 2.128\,09\,(31)$ fm.

PACS No: 31.30.jr,36.10.Ee,42.62.Fi,14.20.Dh

Résumé : La longue quête d'une mesure du décalage de Lamb dans l'hydrogène muonique est terminée. L'an dernier, nous avons mesuré la séparation en énergie $2S^{F=1}_{1/2}$–$2P^{F=2}_{3/2}$ dans μp (Pohl et al., *Nature*, **466**, 213 (2010)) avec une précision expérimentale de 15 ppm, deux fois meilleure que notre objectif initial. Utilisant des calculs QED contemporains des contributions fines, hyperfines, QED et de dimension finie, nous obtenons une valeur quadratique moyenne du rayon de charge du proton égale à $r_p = 0{,}841\,84\,(67)$ fm. Cette valeur est 10 fois plus précise, mais 5 déviations standard moindre que la valeur CODATA 2006 pour r_p. L'origine de ce désaccord reste inconnue. Notre mesure, avec des mesures précises de la transition 1S–2S dans l'hydrogène et le deutérium ordinaires, donne de meilleures valeurs pour la constante de Rydberg, $R_\infty = 10\,973\,731{,}568\,160\,(16)$ m^{-1} et pour le rayon de charge du deutéron $r_p = 2{,}128\,09\,(31)$ fm.

[Traduit par la Rédaction]

Received 7 August 2010. Accepted 29 November 2010. Published on the NRC Research Press Web site at cjp.nrc.ca on 19 January 2011.

R. Pohl,[2] A. Antognini, and T. Nebel. Max-Planck-Institut für Quantenoptik, 85748 Garching, Germany.
F. Nez, F. Biraben, P. Indelicato, L. Julien, E.-O. LeBigot, and C. Schwob. Laboratoire Kastler Brossel, École Normale Supérieure, CNRS and Université P. et M. Curie, 75252 Paris, CEDEX 05, France.
F.D. Amaro, J.M.R. Cardoso, L.M.P. Fernandes, J.A.M. Lopes, C.M.B. Monteiro, and J.M.F. dos Santos. Departamento de Física, Universidade de Coimbra, 3004-516 Coimbra, Portugal.
D.S. Covita and J.F.C.A. Veloso. I3N, Departamento de Física, Universidade de Aveiro, 3810-193 Aveiro, Portugal.
A. Dax and S. Dhawan. Physics Department, Yale University, New Haven, CT 06520-8121, USA.
A. Giesen and K. Schuhmann. Dausinger & Giesen GmbH, Rotebühlstr. 87, 70178 Stuttgart, Germany.
T. Graf. Institut für Strahlwerkzeuge, Universität Stuttgart, 70569 Stuttgart, Germany.
T.W. Hänsch. Max-Planck-Institut für Quantenoptik, 85748 Garching, Germany; Ludwig-Maximilians-Universität, Munich, Germany.
C.-Y. Kao and Y.-W. Liu. Physics Department, National Tsing Hua University, Hsinchu 300, Taiwan.
P. Knowles, L. Ludhova, F. Mulhauser, and L.A. Schaller. Département de Physique, Université de Fribourg, 1700 Fribourg, Switzerland.
P. Rabinowitz. Department of Chemistry, Princeton University, Princeton, NJ 08544-1009, USA.
D. Taqqu. Paul Scherrer Institut, 5232 Villigen-PSI, Switzerland.
F. Kottmann. Institut für Teilchenphysik, ETH Zürich, 8093 Zürich, Switzerland.

[1]This paper was presented at the International Conference on Precision Physics of Simple Atomic Systems, held at École de Physique, les Houches, France, 30 May – 4 June, 2010.

[2]Corresponding author (e-mail: randolf.pohl@mpq.mpg.de).

1. Introduction

The observation of Lamb and Retherford [1] that the $2S_{1/2}$ and $2P_{1/2}$ levels in atomic hydrogen (H) are separated by the famous "1000 Mc/sec" marks a cornerstone of modern physics. Shortly afterwards, Bethe [2] explained the splitting by what is now called the "self-energy" (SE) of the electron. Uehling's "vacuum polarization" (VP) [3] is too small and has the wrong sign to explain Lamb's observation.

The initial motivation for a measurement of the Lamb shift in muonic hydrogen (μp, the exotic hydrogen atom made from a proton and a negative muon μ^-) was to study VP [4]. VP does of course also contribute to the Lamb shift in ordinary hydrogen, but in μp, VP is the dominant contribution. This is due to the fact that the mass of the muon is 207 times the mass of the electron, and hence the Bohr orbit in muonic hydrogen is smaller by $\mu_{\mu p}/\mu_H \approx 186$, where $\mu_{\mu p}$ and μ_H are the reduced masses of the μp and H atoms (H = *e*p), respectively.

In addition, the large reduced mass results in a strong enhancement of the effect of the finite size of the proton on the S levels. The finite size effect depends on the overlap of the muon wave function with the proton charge distribution, and scales with the third power of the reduced mass. The finite size effect on the 2S state in muonic hydrogen is as much as 2% of the total Lamb shift (Fig. 1).

1.1 X-rays from muonic hydrogen

The first X-rays from muonic hydrogen atoms were observed in 1970 [5], and the search for the metastable 2S state began. This state is crucial for Lamb shift measurement where one aims to create μp atoms in the 2S state, drive the 2S–2P transition using a laser pulse around $\lambda = 6$ μm, and observe the laser-induced Lyman-α X-rays at 1.9 keV (Fig. 2*b*) (1 bar = 100 kPa).

However, stopping muons in H_2 creates μp atoms in a high principal quantum number $n \approx 14$ [6], [7]. The vast majority of these atoms de-excite to the 1S ground state and are hence of no use for the laser experiment. Furthermore, this de-excitation happens also via emission of Lyman-α, β, γ, ... X-rays (Fig. 2*a*), and this creates a severe background at "prompt" times, i.e., at the time of μp (1S or 2S) formation.

A way out is to fire the laser pulse at "delayed" times, i.e., a few hundred nanoseconds after the prompt muonic cascade is over, to avoid the prompt background. This then defines two crucial requirements for the feasibility of the laser experiment: (*i*) The μp (2S) population must be "sufficiently high", i.e., at least about 1% of all muons should form μp (2S) states and (*ii*) the 2S lifetime should be "sufficiently long", i.e., the few hundred ns required to avoid the prompt Lyman X-rays.

1.2 Search for the 2S state

The fraction of muons reaching the 2S state during the prompt cascade, ϵ_{2S}^{total}, was deduced between 1977 and 1984 from the measurement of K-line intensity ratios [8–10]: at low H_2 gas pressures, the *n*P states with $n \geq 3$ decay mostly radiatively to the 1S ground state or to the 2S metastable state. Therefore, one can calculate the number of μp (2S) atoms by observing the atoms reaching the 1S state, by counting the number of K_α, K_β, K_γ, etc., X-rays (the so-called "K-line intensities"),

$$\epsilon_{2S}^{total} = 0.134 \frac{I_{K_\beta}}{I_{K_{tot}}} + 0.144 \frac{I_{K_{>\beta}}}{I_{K_{tot}}}$$

Here, $I_{K_{tot}} = I_{K_\alpha} + I_{K_\beta} + I_{K_\gamma} + \cdots$ is the total number of K X-rays. The calculated [11] radiative branching ratio $3P \rightarrow 2S/3P \rightarrow 1S$ is 0.134, and the average branching ratio for $n > 3P$ states is 0.144.

The X-ray measurements [8–10] determined ϵ_{2S}^{total} at pressure ranges from a fraction of one mbar up to atmospheric pressure. The value of ϵ_{2S}^{total} is as large as 3% at 1 mbar of hydrogen gas pressure (black squares and triangles in Fig. 3).

1.3 2S lifetime

The accepted scenario [17, 18] at that time was that any μp(2S) atom with a kinetic energy (k.e.) below 0.31 eV (which corresponds to the 0.2 eV 2S Lamb shift in the center of mass system) should survive on the order of a thousand collisions before undergoing Stark decay (2S–2P mixing during a collision) to the 1S ground state. This results in a 2S quench rate of less than the muon decay rate at gas pressures well below one bar or so [17, 19, 20]. These slow μp(2S) atoms constitute the so-called "long-lived" μp(2S) population.[3] They should be detectable via the Lyman-α X-rays emitted in the Stark decay.

A series of experiments failed to observe these delayed K_α X-rays and (wrongly) concluded that the long-lived μp (2S) population ϵ_{2S}^{long} was too small for a laser experiment [8–10, 21].

In vacuum, the μp(2S) lifetime is essentially equal to the muon lifetime. Collisional quenching, like the abovementioned Stark decay, can be reduced by working with sufficiently low gas pressures, below a mbar or so. Therefore, we developed methods like frictional cooling of the muon beam [22] and muon trapping in electric fields [23], which ultimately allowed us to stop muons in 0.06 mbar H_2 gas at room temperature, and in a volume small enough to be illuminated by a laser [24].

We determined the k.e. of μp atoms formed after muon stop in H_2 gas at pressures between 0.06 and 16 mbar [13], and we indeed observed a sizeable amount of μp atoms with k.e. *below* the 0.31 eV threshold energy, which leads to μp(2S) longevity [6, 7, 18]. We concluded that $\epsilon_{2S}^{long} \approx 1\%$ (see red open circles in Fig. 3), which was in severe contradiction to the much lower upper limits of ϵ_{2S}^{long} given by the above mentioned non-observation of X-rays from Stark decay [8–10, 21].

We could finally resolve this contradiction by the first direct observation of *non*-radiatively quenched long-lived μp(2S) atoms [13–15]; in a collision, radiationless Coulomb de-excitation takes place either via intermediate molecule formation [25, 26] or without [27]. Either way, the 2S binding energy of 1.9 keV is shared among a formed μp(1S)

[3] In contrast, the "short-lived" μp (2S) population [16] is made from the fast μp (2S) atoms with a k.e. larger than 0.31 eV, which can be transferred to the 2P state within a single collision.

Fig. 1. The $n=2$ levels in muonic hydrogen. Vacuum polarization dominates the 2S Lamb shift of 202 meV. The finite size effect is as much as 2% of the total Lamb shift. The first transition we have measured in muonic hydrogen is indicated in green (light grey in print version): $2S^{F1}_{1/2}$–$2P^{F2}_{3/2}$. The 1S ground state is 1.9 keV below the $n=2$ states plotted here.

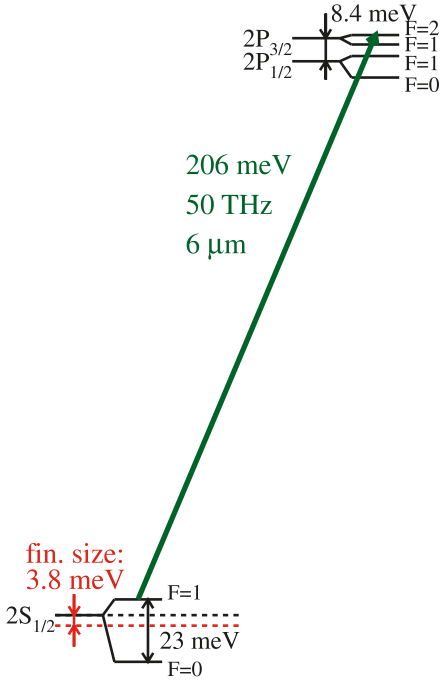

Fig. 2. Experimental principle. (left) 99% of the muons stopped in H_2 gas at 1 mbar pressure proceed directly to the 1S ground state, thereby emitting X-rays of the Lyman series of around 2 keV. One percent of the muons form long-lived metastable 2S states with a lifetime $\tau_{2S}=1$ μs at 1 mbar. (right) Laser light of suitable wavelength around $\lambda=6$ μm drives the 2S-2P transition. The 2P state de-excites within 8 ps to the 1S ground state via emission of a Lyman-α X-ray at 1.9 keV.

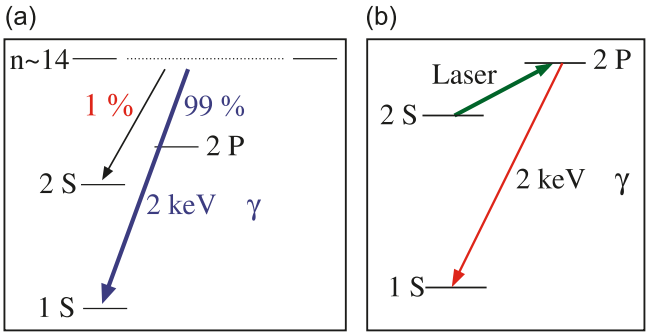

atom and one proton of a colliding H_2 molecule. We observed [14] the μp(1S) atoms with 0.9 keV k.e., and deduced $\epsilon_{2S}^{long} \approx 1\%$ [14, 15], in agreement with our previously extracted values (see full circles in Fig. 3). The Coulombic de-excitation limits the lifetime of the long-lived 2S states to about 1 μs at 1 mbar gas pressure [15].

2. The laser spectroscopy experiment

A long-lived fraction $\epsilon_{2S}^{long} \approx 1\%$ and a lifetime $\tau_{2S} \approx 1$ μs at 1 mbar are sufficient for a laser experiment

Fig. 3. Total, long-lived, and short-lived 2S population [12]. (black triangles/squares) Total μp(2S) population ϵ_{2S}^{total} from measured X-ray yields [8–10]. (red circles, dark grey in print) Long-lived μp(2S) population ϵ_{2S}^{long} from μp (1S) TOF, both (open circles) indirectly determined [13] and (solid dots) directly observed [13–15]. (blue star, light grey in print) Short-lived μp(2S) population ϵ_{2S}^{short} from delayed K_α X-rays [16]. ϵ_{2S}^{short} is plotted as a difference from ϵ_{2S}^{total} to indicate the remaining ϵ_{2S}^{long}.

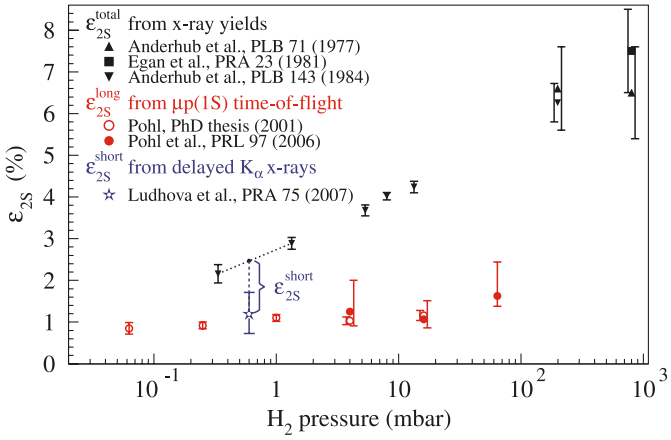

[28]. The proposal "R98-03" was accepted at PSI [29] in early 1999, and the development of the setup began [30–34].

The principle of the experiment (Fig. 2) is to stop muons in H_2 gas and drive the 2S–2P transition with a pulsed laser tunable around $\lambda=6$ μm. Lyman-α X-rays at 1.9 keV, which appear in coincidence with the laser pulse are the signature of a successful 2S–2P transition. We have finally observed 6 events per hour on resonance, on top of 1 background event per hour (Figs. 4 and 5), and could measure the $2S^{F=1}_{1/2}$ to $2P^{F=2}_{3/2}$ transition frequency in μp to be 49 881.88 (76) GHz [38].

2.1 Low energy negative muon beam line

The low-energy muon beam line [39] was designed and built at PSI, Switzerland [40]. An overview is shown in Fig. 6, and the details of the final stages are given in Fig. 7.

The novel beamline [41] consists of the "cyclotron trap" (CT), the "muon extraction channel" (MEC), and the 5 T solenoid containing the elements depicted in Fig. 7. The CT acts here as a magnetic bottle made from two 4 T ring coils, with $B=2$ T in the center of the CT. Negative pions enter the CT tangentially at the rate of 10^8 sec^{-1} and are moderated in a degrader to bring them onto suitable orbits. About 30% of the pions decay into μ^-, which are further decelerated by repeatedly passing a metallized thin Formvar foil placed in the center of the CT. This foil is kept at –20 kV potential. The μ^- are confined in the magnetic bottle until this repulsive electric field dominates over the magnetic forces. Muons leave the CT close to the axis and enter the MEC, a toroidal momentum filter (magnetic field $B=0.15$ T), which favors muons with ~20 keV/c momentum and separates them from background radiation. From the MEC, the muons are guided into the bore hole of a 5 T superconducting magnet, slightly above its axis. The high magnetic field of the solenoid ensures a small radial size of the muon beam, thereby reducing the target volume to be illuminated by the laser. Before entering the hydrogen target,

Fig. 4. Summed X-ray time spectra recorded in 2009, (top) on resonance and (bottom) off resonance (see Fig. 5). The insets show the same data. The laser light illuminates the muonic atoms at times $t \in [0.887, 0.962]$ μs (indicated in red).

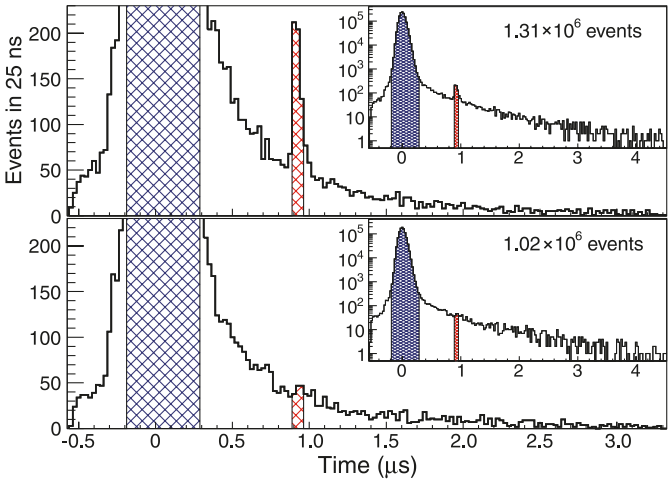

Fig. 5. The resonance measured in 2009, a water absorption measurement used for calibration and the predicted line positions using the proton rms charge radius from electron scattering [35, 36] or CODATA [37].

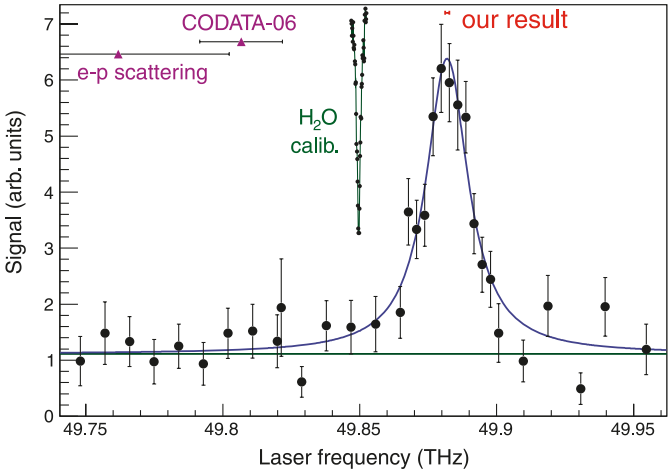

the muons pass two stacks of ultra-thin carbon foils (area density d = 4 μg/cm^2), kept at high electric potential, which both serve as muon detectors and decelerate the muons to 3–6 keV. Each muon releases a few electrons in the stack-foils, which are separated from the much slower muons in an $\boldsymbol{E} \times \boldsymbol{B}$ separator field. The electrons are detected by plastic scintillators and photomultiplier tubes and provide the trigger signal for the data acquisition system and the laser.

Finally, the muons arrive in the gas target that is filled with 1.0 hPa of H_2 gas at room temperature and has a length of 20 cm along the beam axis. The transverse dimensions of the stop volume are 5 mm × 12 mm. Roughly half of the muons stop inside the volume, which is later illuminated by the laser light.

2.2 Laser system for λ = 6 μm

The design of the laser system [42, 43] is dictated by the nature of the muon beam and the lifetime of the 2S state

Fig. 6. Low-energy negative muon beam line. Negative pions are injected into the cyclotron trap (CT) and decay into muons, which are decelerated and leave the CT axially. The muon extraction channel (MEC) removes unwanted background radiation (electrons, gamma rays, neutrons). The muons then enter the final 5 T solenoid, where the experiment takes place (Fig. 7).

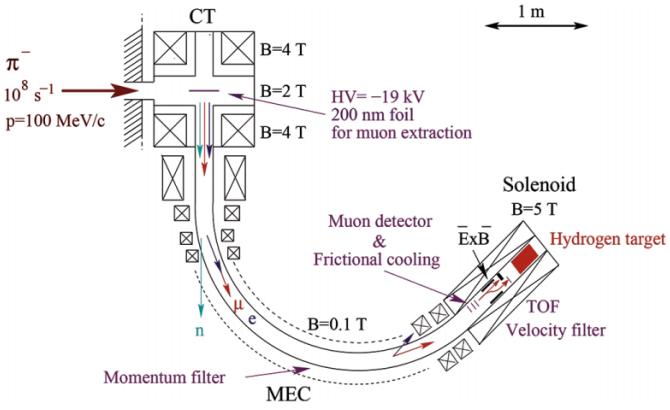

Fig. 7. Final stages of the muon beam line. Slow μ^- enter the 5 T solenoid from left. They traverse two stacks $S_{1,2}$ of ultra-thin carbon foils, where a few electrons are ejected and accelerated by an applied high voltage (HV). The e^- are detected in plastic scintillators, read out by photo multipliers ($PM_{1–3}$). A capacitor just behind S_1 separates e^- from μ^- by a vertical $\boldsymbol{E} \times \boldsymbol{B}$ drift. The delayed coincidence [PM_1 AND (PM_2 OR PM_3)] triggers the laser system (Fig. 8). The muon stops inside the gas target filled with 1 mbar of H_2 gas. The stop volume is illuminated by the laser pulse injected into a multi-pass cavity (Fig. 9).

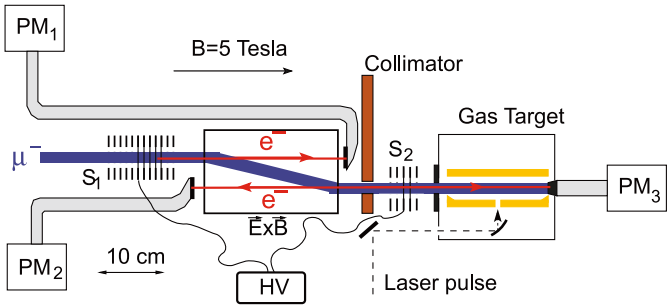

$\tau_{2S} \approx 1$ μs in 1 mbar of H_2 gas. The muons arrive at random times with an average rate of ∼600 s^{-1}. The S_1–S_2 coincidence criterion, together with the respective efficiencies, results in up to 400 s^{-1} muon triggers. The laser system has to be *stochastically* triggerable on the arrival of a single muon, and it has to produce pulses tunable around λ = 6 μm, with a delay (trigger pulse to light output) of less than 1 μs (given by the 2S lifetime).

The laser system [42, 43] is depicted in Fig. 8. Two parallel, continuously pumped Yb:YAG disk lasers [44], each made from an oscillator, an amplifier, and subsequent second harmonic generation (SHG) in LBO, provide the pump energy for a titanium sapphire (TiSa) laser system.

Initially we had used an Excimer-pumped dye laser [42] system instead of the Yb:YAG disk laser, but this resulted in long internal delays (1200 ns of the Excimer lasers), low repetition rates (100 Hz), and low uptime due to frequent dye changes.

Fig. 8. Laser system. For details see text.

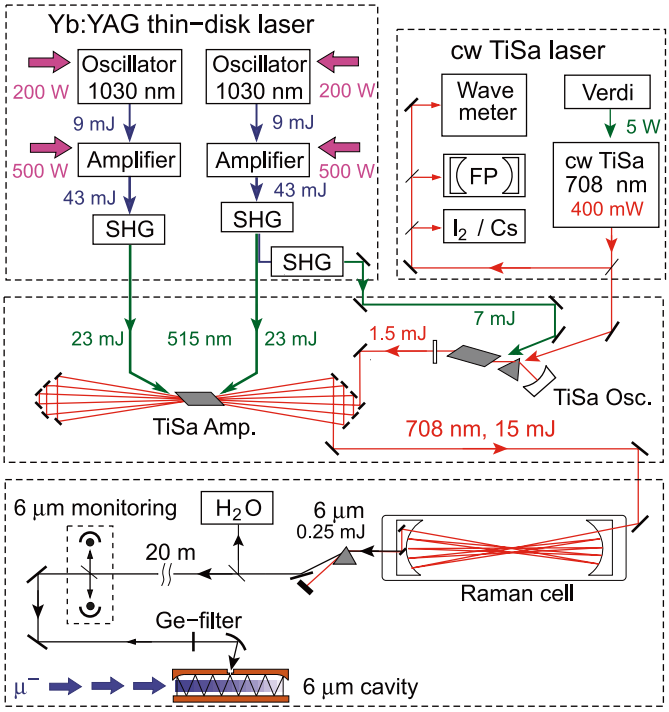

The disk laser technology was one key to the success of the experiment in 2009. The all solid-state design of the laser resulted in nearly 100% up-time over the several weeks of data acquisition. Moreover, pumping the Yb:YAG lasers continuously with up to 1.4 kW of cw pump power ensures a short internal delay of about 250 ns between muon trigger and pulse output from the Yb:YAG oscillators. After SHG, as much as 53 mJ of green pulse energy at $\lambda = 515$ nm is available.

The pulsed TiSa laser consists of an oscillator, providing 1.5 mJ of tunable red light around $\lambda = 708$ nm, followed by a multi-pass amplifier, which boosts the pulse energy to 15 mJ. A pulse length of ~ 5 ns, given by the TiSa oscillator length and some pulse shortening inside the TiSa amplifier, is optimal for subsequent efficient Raman–Stokes conversion in a high-pressure H_2 Raman cell [45]. Here, three subsequent vibrational Stokes shifts (4155.22(2) cm^{-1}) in 15 bar of H_2 convert the pump pulses at $\lambda = 708$ nm via 1.0 and 1.7 µm to the desired 6 µm wavelength.

We obtained pulses of 0.25 mJ at 6 µm, which we separated from the various other wavelengths (pump light and light from vibrational and rotational Stokes and anti-Stokes of different order) first by a CaF_2 prism, and further by a Ge window anti-reflection coated for 6 µm. The 6 µm infrared (IR) light is easily absorbed by water vapor in air. Therefore, the IR light was sent from the laser hut to the muon beam area through an evacuated tube of ~ 12 m length. Before and after the tube, the IR light was transported in a dry N_2 atmosphere using N_2 gas from a LN_2 dewar. About 0.1 mJ of the 6 µm light reached the entrance of the target cavity.

The target cavity is depicted in Fig. 9. It was designed to illuminate the elongated muon stop volume (175 mm along the beam axis, 5 mm in height, and about 15 mm in width) from the side. In addition, we wanted to avoid any active

Fig. 9. Multipass target cavity. Horizontal plane (left), vertical plane, perpendicular to the muon beam (right).The entrance mirror (bottom) is a flat central part with attached cylindrical pieces. The light can enter through a 0.6 mm diameter hole in the center of the flat part. The attached cylinders ensure the horizontal confinement of the light. The vertical confinement is done by the curvature of the cylindrical mirror (top). A 90° off-axis parabolic mirror helps to inject the light using a mirror in the laser hut, placed 20 m away.

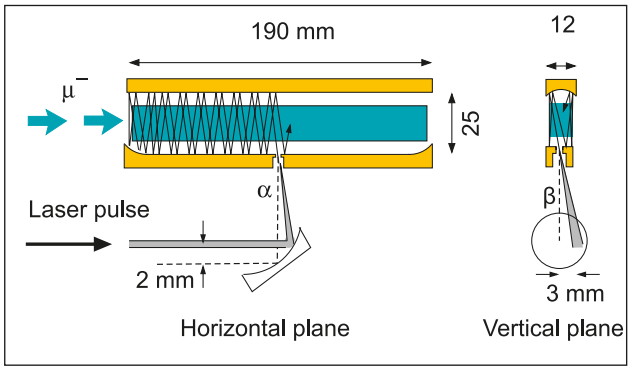

mirror stabilization in the H_2 target gas and in the 5 T magnetic field. This was accomplished by a robust design using a flat entrance mirror with cylinder pieces attached for the horizontal confinement and an opposing cylindrical mirror for vertical confinement. Injection of the 6 µm light was ensured by an off-axis parabolic mirror that focused the light through a 0.6 mm diameter injection hole in the flat part of the entrance mirror. Off-center injection enabled illumination of a large volume. The final Ge/ZnS HR coating with $R \approx 99.89\%$ reflectivity resulted in an enhancement factor of several hundred. 0.1 mJ of light injected into the cavity did therefore result in a 30% transition probability on the center of the resonance.

Frequency control of the laser system works as follows. The pulsed TiSa oscillator is injection seeded by cw light from a single frequency cw TiSa ring laser. The cw TiSa is at all times locked to a transmission peak of a stable Fabry–Perot (FP) reference cavity with a free spectral range (FSR) of 1497.332(3) MHz.

The pulsed TiSa system follows the laser frequency of the cw TiSa, apart from a measured chirp [42] of about 0.1 GHz. The three sequential Stokes shifts inside the Raman cell remove a constant energy of 3 times the vibrational $v = 0 \rightarrow 1$ separation in H_2 from each photon. As a consequence, a detuning of the cw TiSa by a frequency $\Delta\nu$ results in *the same* detuning $\Delta\nu$ of the laser frequency at 6 µm.

The laser wavelength at 6 µm is of course well-known from the measured wavelength of the cw TiSa laser and the known Raman shift, with a small correction due to the measured chirp in the pulsed TiSa oscillator and amplifier. However, to minimize systematic uncertainties, we performed the laser frequency calibration directly at $\lambda = 6$ µm by means of water vapor absorption in air and in a cell. The absolute position of the water absorption lines have been measured [46] to an absolute precision of 1 MHz, and they are tabulated in the HITRAN database [47]. The total scan range is within less than 100 FSR of the FP, so the 3 kHz uncertainty of the FSR determination by I_2, Rb, and Cs spectroscopy is negligible.

The FSR of the FP cavity defines the grid of measurement points of the muonic transition, which has a natural line width of $\Gamma_{2S-2P} = 18.6$ GHz. The search for the resonance line was performed at every sixth FP fringe, and the final scan of the resonance was done at every other FP fringe (see Fig. 5).

2.3 Detectors for 1.9 keV X-rays

Initially we envisaged gas-scintillation proportional counters (GSPC), read out by CsI-coated micro-strip gas chambers (MSGC) [48], but these were then replaced by large-area avalanche photodiodes (LAAPDs) [49–53]. These have an active surface of 13.5 mm × 13.5 mm, with only very little insensitive surface. They work very well in our strong magnetic field of 5 T [50]. To improve the energy resolution and the signal-to-noise ratio, the LAAPDs are cooled to –30 °C. Their typical time and energy resolutions for 1.9 keV X-rays are 35 ns and 25% (full-width at half maximum), respectively. Ten LAAPDs were mounted above, and 10 below, the muon stop volume inside the target, only 8 mm away from the muon beam center. This resulted in a solid angle coverage of about 20% of 4π. The LAAPDs have been optimized for the detection of the 1.9 keV X-rays from the μp (2P→1S) transition, but they are also sensitive to the muon decay electrons. In addition, plastic scintillators have been installed to increase the detection efficiency for decay electrons, whose appearance with some delay following a 2 keV X-ray signal is required in the data analysis to reduce the background. The LAAPD signals are read out using VME waveform digitizers.

Accumulated time spectra on and off resonance are shown in Fig. 4. The laser-induced peak is clearly visible when the laser is tuned to the correct frequency.

3. Results

3.1 The experiment saga

Our first "machine development" beam time took place in 2002. We put together all parts of the experiment and managed to run for a few hours before the end of the beam time. We identified several weak points of the apparatus and changed them before our first real data acquisition run in 2003. The 50 Hz XeCl Excimer laser was replaced by two XeCl Excimer lasers capable of 100 Hz repetition rate. The internal delay of the Excimer lasers could be shortened to 1200 ns. Two parallel dye MOPA systems provided up to 90 mJ of green pump power for the TiSa system. We also replaced the LAAPDs to achieve a larger solid angle and installed a muon-anticoincidence detector at the end of the gas target to veto laser shots when the muon did not stop inside the gas target.

After three weeks of data acquisition in 2003 the result was very disappointing (Fig. 10). No sign of a resonance could be observed within the "reasonable range" of ±3σ of the prediction using the CODATA value [37] of the proton rms charge radius at FP = 842. We explained the lack of signal with a too long internal delay of the laser system [41]. Now we know better. We spent most of the measurement time around FP = 842, but the peak was finally found in 2009 at FP = 895, at which we had not measured for a long enough time in 2003. In hindsight, of course, one can identify the two right-most points in Fig. 10, which are somewhat higher than the background, with the peak finally observed in 2009.

Fig. 10. No resonance was observed in 2003. The *x*-axis shows the laser frequency in FP fringe numbers of 1497 MHz with an offset of 282 000. The dashed horizontal line indicates the measured background level. Using the CODATA value of r_p we expected a resonance at FP = 842, but we found it at FP = 895 in 2009.

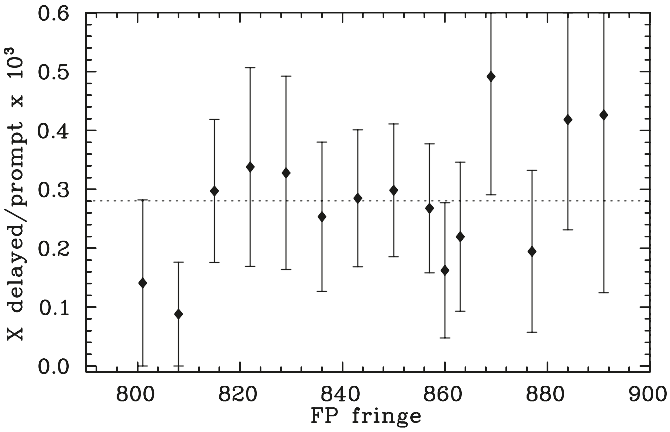

After the development of the Yb:YAG disk lasers [42, 43], we had another beam time in 2007. Again, we searched for the resonance in the "reasonable" range, but serious technical problems prevented us from taking sufficient data.

We seemed to observe an "indication of a signal", but this was most probably due to background created by the laser system, plasma formation when the tightly focused beam hit the injection hole of the target cavity (Fig. 9). We observed a similar effect in 2009 but could understand the problem and solve it by additional shielding of the X-ray detectors against visible light and by anti-coincidence detectors, which warned us when a plasma was created because of laser misalignment.

The 2007 beam time did however have its successes: We increased the muon rate and decreased the background level, as is apparent from Figs. 10 and 11. The disk laser had a much shorter internal delay than the previously used Excimer lasers.

After 1 week of data taking in 2009, again in the "reasonable range" around the CODATA prediction, we had again no sign of a resonance and hence decided to extend the search region. Finally, we found the peak 5σ away from the predicted position using the CODATA rms proton charge radius.

3.2 Lamb shift in muonic hydrogen

The final results of the 1st resonance observed in muonic hydrogen have been published recently [38]. The center of the $2S_{1/2}^{F=1}$ to $2P_{3/2}^{F=2}$ transition in μp is at 49 881.88 (76) GHz. The uncertainty of 15 ppm is twice better than our goal presented in the proposal [29]. It consists of 700 MHz statistical uncertainty from the free fit of a Lorentzian resonance line on top of a flat background and the 300 MHz total systematic uncertainty, which is exclusively due to our laser wavelength calibration procedure using water vapor absorption lines. The absolute line position is known to 1 MHz [46, 47], but pulse to pulse instabilities of our laser system limits the frequency determination to 300 MHz uncertainty.

Fig. 11. Result of the 2007 beam time. The *x*-axis is in the same units as in Fig. 10, but with an offset of 800; the expected position is FP = 42. The apparent indication of a resonance was most probably induced background (see text). The peak would have been at FP = 95, but we did not search there; the rightmost point FP = 78 corresponds to roughly 49.86 THz (see Fig. 5).

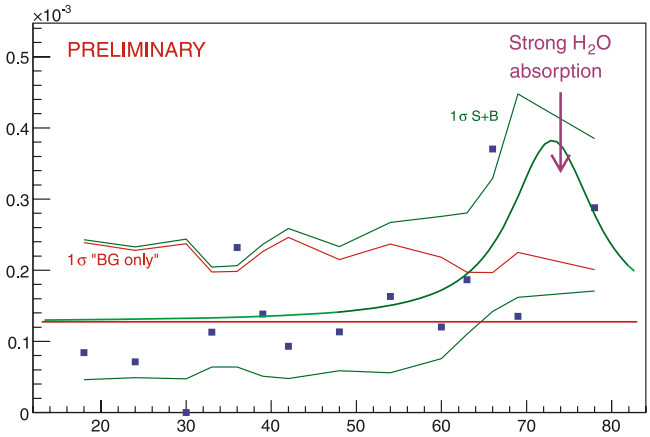

Other systematic effects that we have considered are Zeeman shift in the 5 T field (<30 MHz), AC and DC Stark shifts (<1 MHz), Doppler shift (<1 MHz), and pressure shift (<2 MHz). Molecular effects do not influence our resonance position, because the formed muonic molecules $pp\mu^+$ are known to de-excite quickly [54] and do not contribute to our observed signal. Also, the width of our resonance line of 18.0(2.2) GHz agrees with the expected width of 20(1) GHz, whereas molecular lines would be wider. The free fit gives $\chi^2 = 28.1$ for 28 degrees of freedom. The resonance position corresponds to an energy of $\Delta\tilde{E} = 206.2949(32)$ meV (see eq. 1).

3.3 The charge radius of the proton

The $2S^{F=1}_{1/2}$–$2P^{F=2}_{3/2}$ energy difference $\Delta\tilde{E}$ in muonic hydrogen is the sum of radiative, recoil, and proton structure contributions, and the fine and hyperfine splittings for our particular transition, and it is given [55–60] by,

$$\Delta\tilde{E} = 209.9779(49) - 5.2262r_p^2 + 0.0347r_p^3 \text{ meV} \quad (1)$$

where

$$r_p = \sqrt{\langle r_p^2 \rangle}$$

is given in fm. The uncertainty of 0.0049 meV in $\Delta\tilde{E}$ is dominated by the proton polarizability term [58] of 0.015(4) meV. A detailed derivation of (1) is given in the Supplementary Information of [38].

We deduce a value of the rms charge radius of the proton of

$$r_p = 0.841\,84(36)(56) \text{ fm} \quad (2)$$

where the first and second uncertainties originate from the experimental uncertainty of 0.76 GHz and the uncertainty in the first term in (1), respectively. Theory, mainly the proton polarizability, gives the dominant contribution to our total relative uncertainty of 8×10^{-4}. Our experimental precision would suffice to deduce r_p to a relative uncertainty of 4×10^{-4}.

3.4 The proton radius puzzle

This new value of the proton radius $r_p = 0.841\,84\,(67)$ fm is 10 times more precise, but 5.0σ smaller, than the previous best (CODATA) value $r_p = 0.876\,8\,(69)$ fm [37], which is mainly obtained from spectroscopy in regular hydrogen (H). It is 26 times more accurate, but 3.1σ smaller, than the previously accepted hydrogen-independent value extracted from electron proton scattering [35, 36] of $r_p = 0.895(18)$ fm. Furthermore, Bernauer et al. have recently published [61] a more precise charge radius of the proton $r_p = 0.879(8)$ fm, using new data from the Mainz MAMI electron accelerator. This new electron scattering value agrees with the one obtained from H/D spectroscopy $r_p = 0.876(8)$ fm (see [37], Table XLV, adjustment 7).

Recent lattice QCD calculations [62], on the other hand, obtain $r_p = 0.83(3)$ fm, favoring a lower radius than the one from H or electron scattering. Also, dispersion analysis of the nucleon form factors has recently [63] also produced smaller values of $r_p \in [0.822 \cdots 0.852]$ fm, in agreement with our accurate value. The situation is summarized in Fig. 12.

3.5 A new value of the Rydberg constant

Assuming for now the correctness of the QED calculations in hydrogen [57, 64] and μp [55, 56, 58–60], we can use our most precise value of r_p and the most accurately measured transition frequency in hydrogen (1S–2S) [65, 66] to deduce a new value of the Rydberg constant,

$$R_\infty = 10\,973\,731.568\,160(16)\,\text{m}^{-1} \quad (3)$$

This is –110 kHz/c or 4.9σ away from the CODATA value [37], but 4.6 times more precise [1.5 parts in 10^{12}]. The new determination continues the astonishing improvement in the accuracy of the most accurately determined fundamental physical constant (Fig. 13).

3.6 The charge radius of the deuteron

The precise measurement of the isotope shift of the 1S–2S transition in regular hydrogen and deuterium atoms [67] gives a very accurate value for the *difference* of the squared charge radii of the proton and the deuteron, $r_d^2 - r_p^2 = 3.820\,07\,(65)$ fm^2. Using this and our precise value of the proton charge radius, we obtain for the rms charge radius of the deuteron,

$$r_d = 2.12809(31)\,\text{fm} \quad (4)$$

This value is within 0.2σ of the value $r_d = 2.130(10)$ fm obtained in electron scattering [68], but 27 times more precise. It is 10 times more precise than the CODATA value of r_d, and 3σ away from it.

4. Conclusions and Outlook

The world's most precise value of the rms proton charge radius $r_p = 0.841\,84\,(67)$ fm, which we have obtained from laser spectroscopy of the Lamb shift in muonic hydrogen

Fig. 12. Our new value $r_p = 0.841\,84\,(67)$ fm from μp spectroscopy [38] disagrees with the values extracted from hydrogen spectroscopy ([37], Table XLV, adjustment 7), the world average from electron scattering [35, 36], and the new electron scattering value from Mainz [61]. The lattice QCD value is from [62], and the dispersion value is from [63].

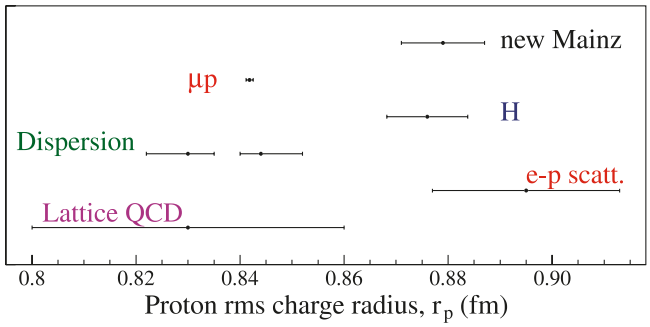

Fig. 13. The Rydberg constant is a corner stone of the CODATA adjustment of fundamental constants [37]. Its accuracy is now 1.5 parts in 10^{12}.

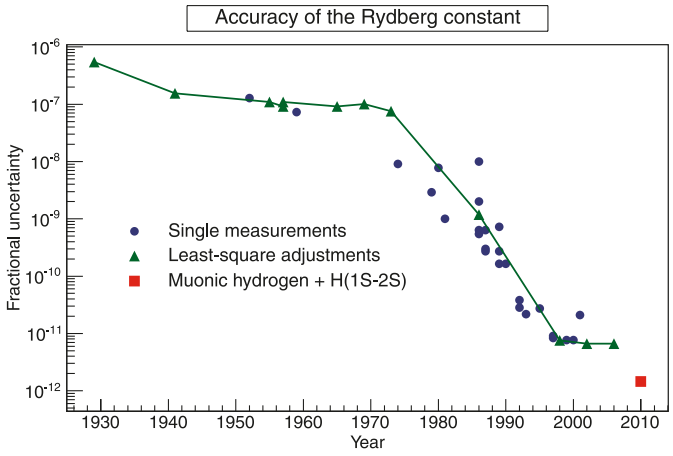

μp, has created a puzzle. The disagreement with the previous values from hydrogen spectroscopy and electron scattering is stunning.

We are confident that the re-evaluation of bound-state QED calculations may soon resolve the puzzle. New insight may also arise from our future project, the measurement of the Lamb shift in the muonic helium ion [69].

References

1. W.E. Lamb and R.C. Retherford. Phys. Rev. **72**, 241 (1947). doi:10.1103/PhysRev.72.241.
2. H.A. Bethe. Phys. Rev. **72**, 339 (1947). doi:10.1103/PhysRev.72.339.
3. E. Uehling. Phys. Rev. **48**, 55 (1935). doi:10.1103/PhysRev.48.55.
4. A. Di Giacomo. Nucl. Phys. B, **11**, 411 (1969). doi:10.1016/0550-3213(69)90090-X.
5. A. Placci, E. Polacco, E. Zavattini, and K. Ziock. Phys. Lett. B, **32**, 413 (1970). doi:10.1016/0370-2693(70)90511-3.
6. T.S. Jensen and V.E. Markushin. Eur. Phys. J. D, **21**, 261 (2002). doi:10.1140/epjd/e2002-00207-y.
7. T.S. Jensen and V.E. Markushin. Eur. Phys. J. D, **21**, 271 (2002). doi:10.1140/epjd/e2002-00208-x.
8. H. Anderhub, H. Hofer, F. Kottmann, P.L. Coultre, D. Makowiecki, O. Pitzurra, B. Sapp, P. Seiler, M. Wälchli, D. Taqqu et al. Phys. Lett. B, **71**, 443 (1977). doi:10.1016/0370-2693(77)90263-5.
9. P.O. Egan, S. Dhawan, V.W. Hughes, D.C. Lu, F.G. Mariam, P.A. Souder, J. Vetter, G.Z. Putlitz, P.A. Thompson, and A.B. Denison. Phys. Rev. A, **23**, 1152 (1981). doi:10.1103/PhysRevA.23.1152.
10. H. Anderhub, H.P. von Arb, J. Böcklin, F. Dittus, R. Ferreira Marques, H. Hofer, F. Kottmann, D. Taqqu, and J. Unternährer. Phys. Lett. B, **143**, 65 (1984). doi:10.1016/0370-2693(84)90805-0.
11. A. Bertin, A. Vacchi, and A. Vitale. Lett. Nuovo Cimento, **18**, 277 (1977). doi:10.1007/BF02783444.
12. R. Pohl. Hyperfine Interact. **193**, 115 (2009). doi:10.1007/s10751-009-0054-1.
13. R. Pohl. Ph.D. thesis. ETH Zurich **14096** (2001). Available from http://e-collection.ethbib.ethz.ch/view/eth:23936.
14. R. Pohl, H. Daniel, F.J. Hartmann, P. Hauser, Y.W. Liu, F. Kottmann, C. Maierl, V.E. Markushin, M. Mühlbauer, C. Petitjean, W. Schott, and D. Taqqu. Hyperfine Interact. **138**, 35 (2001). doi:10.1023/A:1020830229258.
15. R. Pohl, H. Daniel, F.J. Hartmann, P. Hauser, F. Kottmann, V.E. Markushin, M. Mühlbauer, C. Petitjean, W. Schott, D. Taqqu, and P. Wojciechowski-Grosshauser. Phys. Rev. Lett. **97**, 193402 (2006). doi:10.1103/PhysRevLett.97.193402. PMID:17155627.
16. L. Ludhova, F.D. Amaro, A. Antognini, F. Biraben, J.M.R. Cardoso, C.A.N. Conde, A. Dax, S. Dhawan, L.M.P. Fernandes et al. Phys. Rev. A, **75**, 040501 (2007). doi:10.1103/PhysRevA.75.040501.
17. R.O. Mueller, V.W. Hughes, H. Rosenthal, and C.S. Wu. Phys. Rev. A, **11**, 1175 (1975). doi:10.1103/PhysRevA.11.1175.
18. G. Carboni and G. Fiorentini. Nuovo Cim. B, **39**, 281 (1977). doi:10.1007/BF02738195.
19. J.S. Cohen and J.N. Bardsley. Phys. Rev. A, **23**, 46 (1981). doi:10.1103/PhysRevA.23.46.
20. L.I. Menshikov and L.I. Ponomarev. Z. Phys. D, **2**, 1 (1986). doi:10.1007/BF01437237.
21. J. Böcklin. Ph.D. thesis, ETH Zurich **7161** (1982).
22. M. Mühlbauer, H. Daniel, F. Hartmann, P. Hauser, F. Kottmann, C. Petitjean, W. Schott, D. Taqqu, and P. Wojciechowski. Hyperfine Interact. **119**, 305 (1999). doi:10.1023/A:1012624501134.
23. H. Daniel, et al. PSI Annual Report. Annex, **1**, 71 (1993).
24. F. Kottmann, H. Daniel, F.J. Hartmann, P. Hauser, C. Maierl, V.E. Markushin, M. Mühlbauer, C. Petitjean, R. Pohl, W. Schott, and D. Taqqu. Hyperfine Interact. **119**, 3 (1999). doi:10.1023/A:1012651231659.
25. P. Froelich and A. Flores-Riveros. Phys. Rev. Lett. **70**, 1595 (1993). doi:10.1103/PhysRevLett.70.1595. PMID:10053335.
26. P. Froelich and J. Wallenius. Phys. Rev. Lett. **75**, 2108 (1995). doi:10.1103/PhysRevLett.75.2108. PMID:10059216.
27. V.P. Popov and V.N. Pomerantsev. nucl-th 0809.0742.
28. D. Taqqu, F. Biraben, C.A.N. Conde, T.W. Hänsch, F.J. Hartmann, P. Hauser, P. Indelicato, P. Knowles, F. Kottmann et al. Hyperfine Interact. **119**, 311 (1999). doi:10.1023/A:1012676517972.
29. P. Hauser, C. Petitjean, L.M. Simons, D. Taqqu, F. Kottmann, R. Pohl, C. Donche-Gay, O. Huot, P. Knowles, F. Mulhauser et al. PSI Proposal R-93.03. 1998.
30. R. Pohl, F. Biraben, C.A.N. Conde, C. Donche-Gay, T.W. Hänsch, P. Hauser, V. Hughes, O. Huot, P. Indelicato, P.

Knowles et al. Hyperfine Interact. **127**, 161 (2000). doi:10.1023/A:1012679114531.
31. F. Kottmann, F. Biraben, C.A.N. Conde, C. Donche-Gay, T.W. Hänsch, F.J. Hartmann, P. Hauser, V. Hughes, O. Huot, P. Indelicato, et al. *In* Quantum electrodynamics and physics of the vacuum. *Edited by* G. Cantatore. Vol. 564 of AIP Conf. Proc. 2001. pp. 13–20.
32. R. Pohl, F. Biraben, C. Conde, C. Donche-Gay, T. Hänsch, F. Hartmann, P. Hauser, V. Hughes, O. Huot et al. Lect. Notes Phys. **570**, 454 (2001). doi:10.1007/3-540-45395-4_29.
33. R. Pohl, A. Antognini, F. Amaro, F. Biraben, J. Cardoso, C. Conde, A. Dax, S. Dhawan, L. Fernandes et al. Can. J. Phys. **83**, 339 (2005). doi:10.1139/p05-016.
34. T. Nebel, F.D. Amaro, A. Antognini, F. Biraben, J.M.R. Cardoso, C.A.N. Conde, A. Dax, S. Dhawan, L.M.P. Fernandes et al. Can. J. Phys. **85**, 469 (2007). doi:10.1139/P07-018.
35. I. Sick. Phys. Lett. B, **576**, 62 (2003). doi:10.1016/j.physletb.2003.09.092.
36. P.G. Blunden and I. Sick. Phys. Rev. C, Nucl. Phys. **72**, 057601 (2005).
37. P.J. Mohr, B.N. Taylor, and D.B. Newell. Rev. Mod. Phys. **80**, 633 (2008). doi:10.1103/RevModPhys.80.633.
38. R. Pohl, A. Antognini, F. Nez, F.D. Amaro, F. Biraben, J.M.R. Cardoso, D.S. Covita, A. Dax, S. Dhawan et al. Nature, **466**, 213 (2010). doi:10.1038/nature09250. PMID: 20613837.
39. P. DeCecco, P. Hauser, D. Horvath, F. Kottmann, L.M. Simons, and D. Taqqu. Nucl. Inst. Methods Phys. Res., Sect. A, **394**, 287 (1997). doi:10.1016/S0168-9002(97)00675-X.
40. F. Kottmann, W. Amir, F. Biraben, C. Conde, S. Dhawan, T. Hänsch, F. Hartmann, V. Hughes, O. Huot et al. Hyperfine Interact. **138**, 55 (2001). doi:10.1023/A:1020886314237.
41. A. Antognini, F.D. Amaro, F. Biraben, U. Brauch, J.M.R. Cardoso, C.A.N. Conde, A. Dax, S. Dhawan, L.M.P. Fernandes, A. Giesen et al. AIP Conf. Proc. **796**, 253 (2005).
42. A. Antognini, F.D. Amaro, F. Biraben, J.M.R. Cardoso, C.A.N. Conde, D.S. Covita, A. Dax, S. Dhawan, L.M.P. Fernandes, T.W. Hänsch et al. Opt. Commun. **253**, 362 (2005). doi:10.1016/j.optcom.2005.04.079.
43. A. Antognini, K. Schuhmann, F.D. Amaro, F. Biraben, A. Dax, A. Giesen, T. Graf, T.W. Hänsch, P. Indelicato et al. IEEE J. Quantum Electron. **45**, 993 (2009). doi:10.1109/JQE.2009.2014881.
44. A. Giesen, H. Hügel, A. Voss, K. Wittig, U. Brauch, and H. Opower. Appl. Phys. B, **58**, 365 (1994).
45. P. Rabinowitz, B. Perry, and N. Levinos. IEEE J. Quantum Electron. **22**, 797 (1986). doi:10.1109/JQE.1986.1073036.
46. R.A. Toth. J. Mol. Spectrosc. **190**, 379 (1998). doi:10.1006/jmsp.1998.7611. PMID:9668030.
47. L.S. Rothman, I.E. Gordon, A. Barbe, D.C. Benner, P.F. Bernath, M. Birk, V. Boudon, L.R. Brown, A. Campargue, J.P. Champion et al. J. Quant. Spectrosc. Radiat. Transf. **110**, 533 (2009). doi:10.1016/j.jqsrt.2009.02.013.
48. M. Boucher, O. Huot, P. Knowles, L. Ludhova, F. Mulhauser, L. Schaller, C. Conde, J. Dos Santos, L. Fernandes, J. Veloso et al. Nucl. Inst. Meth. A, **505**, 136 (2003), 10th Symposium on Radiation Measurements and Applications, Ann Arbor, Michigan, 21–23 May 2002.
49. L. Fernandes, A. Antognini, M. Boucher, C. Conde, O. Huot, P. Knowles, F. Kottmann, L. Ludhova, F. Mulhauser, R. Pohl, et al. Spectrochim. Acta, B At. Spectrosc. **58**, 2255 (2003). doi:10.1016/S0584-8547(03)00214-3.
50. L. Fernandes, A. Antognini, M. Boucher, C. Conde, O. Huot, P. Knowles, F. Kottmann, L. Ludhova, F. Mulhauser, R. Pohl et al. Nucl. Inst. Methods Phys. Res. Sect., A, **498**, 362 (2003). doi:10.1016/S0168-9002(02)02081-8.
51. L. Fernandes, J. Lopes, J. dos Santos, P. Knowles, L. Ludhova, F. Mulhauser, F. Kottmann, R. Pohl, and D. Taqqu. *In* 2003 IEEE Nuclear Science Symposium, Conference Record, Vols. 1–5. *Edited by* S. Metzler. IEEE Nuclear Science Symposium - Conference Record. 2004. pp. 776–779.
52. L.M.P. Fernandes, D.S.A.P. Freitas, A.M.F. Trindade, J.F.C.A. Veloso, C.M.B. Monteiro, L.F.R. Ferreira, and J.M.F. dos Santos. IEEE Trans. Nucl. Sci. **51**, 1509 (2004). doi:10.1109/TNS.2004.832968.
53. L.M.P. Fernandes, F.D. Amaro, A. Antognini, J.M.R. Cardoso, C.A.N. Conde, O. Huot, P.E. Knowles, F. Kottmann, J.A.M. Lopes et al. J. Instrum. **2**, 08005 (2007). doi:10.1088/1748-0221/2/08/P08005.
54. S. Kilic, J.P. Karr, and L. Hilico. Phys. Rev. A, **70**, 042506 (2004). doi:10.1103/PhysRevA.70.042506.
55. K. Pachucki. Phys. Rev. A, **53**, 2092 (1996). doi:10.1103/PhysRevA.53.2092. PMID:9913114.
56. K. Pachucki. Phys. Rev. A, **60**, 3593 (1999). doi:10.1103/PhysRevA.60.3593.
57. M.I. Eides, H. Grotch, and V.A. Shelyuto. Phys. Rep. **342**, 63 (2001) . doi:10.1016/S0370-1573(00)00077-6.
58. E. Borie. Phys. Rev. A, **71**, 032508 (2005). doi:10.1103/PhysRevA.71.032508.
59. A.P. Martynenko. Phys. Rev. A, **71**, 022506 (2005). doi:10.1103/PhysRevA.71.022506.
60. A.P. Martynenko. Phys. At. Nucl. **71**, 125 (2008).
61. J.C. Bernauer, P. Aschenbach, C. Ayerbe Gayoso, R. Böhm, D. Bosnar, L. Debenjak, M.O. Distler, L. Doria, A. Esser, H. Fonvieille, J.M. Friedrich, J. Friedrich, M. Gómez Rodríguez de la Paz, M. Makek, H. Merkel, D.G. Middleton, U. Müller, L. Nungesser, J. Pochodzalla, M. Potokar, S. Sánchez Majos, B.S. Schlimme, S. Širca, Th. Walcher, and M. Weinriefer. Phys. Rev. Lett. **105**, 242001 (2010). doi:10.1103/PhysRevLett.105.242001.
62. P. Wang, D.B. Leineweber, A.W. Thomas, and R.D. Young. Phys. Rev. D Part. Fields Gravit. Cosmol. **79**, 094001 (2009).
63. M.A. Belushkin, H.W. Hammer, and U.G. Meissner. Phys. Rev. C Nucl. Phys. **75**, 035202 (2007).
64. S.G. Karshenboim. Phys. Rep. **422**, 1 (2005). doi:10.1016/j.physrep.2005.08.008.
65. M. Niering, R. Holzwarth, J. Reichert, P. Pokasov, T. Udem, M. Weitz, T.W. Hänsch, P. Lemonde, G. Santarelli, M. Abgrall, P. Laurent, C. Salomon, and A. Clairon. Phys. Rev. Lett. **84**, 5496 (2000). doi:10.1103/PhysRevLett.84.5496. PMID:10990978.
66. M. Fischer, N. Kolachevsky, M. Zimmermann, R. Holzwarth, T. Udem, T.W. Hänsch, M. Abgrall, J. Grünert, I. Maksimovic et al. Phys. Rev. Lett. **92**, 230802 (2004). doi:10.1103/PhysRevLett.92.230802. PMID:15245149.
67. C.G. Parthey, A. Matveev, J. Alnis, R. Pohl, T. Udem, U.D. Jentschura, N. Kolachevsky, and T.W. Hänsch. Phys. Rev. Lett. **104**, 233001 (2010). doi:10.1103/PhysRevLett.104.233001. PMID:20867231.
68. I. Sick and D. Trautmann. Nucl. Phys. A. **637**, 559 (1998). doi:10.1016/S0375-9474(98)00334-0.
69. A. Antognini, F. Biraben, J.M.R. Cardoso, D.S. Covita, A. Dax, L.M.P. Fernandes, A.L. Gouvea, T. Graf, T.W. Hänsch et al. Can. J. Phys. **89**, xxx (2011).